EUROPEAN COMMISSION

Community Research

MATISSE

Materials' Innovations for Safe and Sustainable nuclear in Europe

FP7-Fission-2013
Combination of Collaborative project (CP) and Coordination and Support Actions (CSA)

Grant agreement no: 604862
Start date: 01/11/2013 Duration: 48 Months

Deliverable 2.1.1

Dataset from DFT calculations on solute/solute and defect/solute interaction, small precipitate stability, as well as mobility of solutes

---

MatISSE – Contract Number: 604862

Document title	Dataset from DFT calculations on solute/solute and defect/solute interaction, small precipitate stability, as well as mobility of solutes
Author(s)	P. Olsson (KTH), L. Messina (KTH), M. Nastar (CEA), C. Domain (EDF)
Number of pages	20
Document type	Deliverable
Work Package	2
Document number	D2.11
Issued by	KTH
Date of completion	01/06/2016
Dissemination level	Public

Summary

Electronic structure calculations have been employed in order to determine interaction parameters between defects and solutes in bcc Fe. The solutes considered are the ones commonly found in RPV steels: Cr, Mn, Ni, Cu, Si and P. The point defects considered are vacancies and ⟨110⟩ self-interstitials, and also solute interactions with ⟨111⟩ and ⟨100⟩ SIA loops have been considered. Migration barriers have been also calculated and self-consistent mean field theory has been used to determine diffusion coefficients, flux coupling characteristics and radiation induced segregation trends. The correlation with available experiments is very good. For the solute – loop interactions, a number of solutes do not conform to the extrapolations that can be made from point defect – solute interaction predictions.

Approval

Rev.	Date	First author	WP leader	Project Coordinator
0	06/2016	P. Olsson, KTH 15.06.2016	L. Malerba, SCK•CEN 20.06.2016	A. Michaux, CEA 21/06/2016
			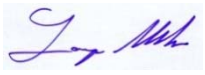	

Distribution list

Name	Organisation	Comments
All beneficiaries	MatISSE	

Table of contents

1. Context and introduction

The main objective of the MEFISTO task is to build knowledge on the effect of the composition on the type of phases that form under irradiation in high-Cr F/M alloys, their kinetics of formation, their effect on radiation-hardening (generally correlated with embrittlement), as a basis for mechanistic embrittlement correlations, similar to those developed for reactor pressure vessel steels used in LWRs. The work proposed is the logical extension and continuation of the work performed in GETMAT [1–3], where the focus was on FeCr alloys of low purity and, particularly, on the formation of Cr-decorated loops as hardening features and on phase transformation kinetics of the alloys under irradiation. Atom Probe Tomography (APT) investigations of the irradiated alloys revealed the presence of other possible hardening features: solute clusters enriched in Cr and in the impurity elements Si, P and Ni.

In order to understand the role of each impurity on the formation of the nano-features formed under irradiation and the eventual synergies between the different species, FeCr(SiNiP) alloys of different composition will be investigated in the framework of the MEFISTO task.

From the modelling point of view, the mechanisms responsible for the formation of the CrMnNiSiP solute clusters have been investigated. These studies have been performed using electronic structure calculations in the framework of density functional theory (DFT) to determine basic interaction parameters and to calculate migration barriers and vibrational/entropic properties. These are then coupled with a self-consistent mean field (SCMF) transport theory framework to determine diffusion coefficients, flux coupling characteristics and radiation induced segregation trends.

The lion share of this work has been published already. For the vacancy-solute interactions and transport properties, see [4] and for the SIA-solute interactions, a manuscript is available in [5].

2. Methods

2.1 Electronic structure methods

The DFT calculations have been performed with the Vienna Ab initio Simulation Package (VASP). The projector augmented wave method (PAW) [6] was applied with the Perdew-Burke-Ernzerhof (PBE) [7] and the Perdew-Wang (PW91) [8] exchange-correlation potentials, with the inclusion of the Vosko-Wilk-Nusair (VWN) [9] spin interpolation of the correlation potential in order to obtain a good description of the magnetism. Supercells of 128 and 250 bcc sites were used with a Monkhorst-Pack 3×3×3 *k*-point grid sampling the Brillouin zone [10] and of 1024 and 1458 bcc sites with gamma point *k*-point representation. The plane wave expansions were cut off at 300 eV. The Methfessel-Paxton broadening scheme is used

with a 0.3 eV width. All relaxations were performed under constant volume conditions. The local magnetic moments are calculated by taking the spin channel difference of the integrated charge density over the Wigner-Seitz sphere of the relevant atom. For the defect – solute and solute – solute interactions the binding energy of a configuration containing the objects A_i is defined as

$$E_b(A_1, A_2, ..., A_n) = \left[E\left(\sum A_i\right) + (n-1)E_{ref}\right] - \sum_i^n E(A_i), \quad (1)$$

where E_{ref} is the energy of the supercell without any objects, $E(A_i)$ is the energy of the supercell containing the single object A_i and $E\left(\sum A_i\right)$ is the energy of the supercell containing all of the interacting objects. With this definition, negative values of E_b denote binding configurations.

The nudged elastic band (NEB) method [11,12], implemented with three images and the climbing-image algorithm [13], was employed for the evaluation of the system energy at the saddle point for all jump configurations. In the climbing image algorithm, three images are sufficient for an accurate evaluation of the saddle-point energy [14,15] since all barriers here investigated are of single-hump shape. The migration barriers are defined as energy difference between the saddle point and the initial state. Each NEB simulation yields the migration energy of a forward jump ($E_{ij}^{\mathrm{mig}} = E_{\mathrm{sad}}^{ij} - E_{\mathrm{relax}}^{i}$) and its backward counterpart ($E_{ji}^{\mathrm{mig}} = E_{\mathrm{sad}}^{ij} - E_{\mathrm{relax}}^{j}$).

The standard potentials available in the VASP library were employed for all involved chemical elements. Concerning the calculations in the Fe(Mn) alloy, it was previously reported that some NEB simulations did not converge to a physically meaningful magnetic state [16] and led to anomalously high migration barriers (>1 eV) [17]. A similar issue was encountered in the Fe(Si) alloy. The system was successfully driven to the correct global minimum with the use of linear mixing in the starting guess of the charge dielectric function, as opposed to using the Kerker model [18,19].

For thermodynamics and stability considerations, about one thousand solute-solute and solute-defect configurations have been considered. For the solute-solute and solute-vacancy configurations, all pairs up to 5nn and triplets up to 2nn have been considered, see Appendix A. For the solute-SIA configurations, configurations with up to two solutes and one SIA have been considered for 0th and 1st shell configurations, see Appendix B.

For the simulations of SIA loop interaction with solutes, elastic corrections were applied using the ANETO code developed by CEA Saclay (SRMP) [20].

2.2 Atomic transport modelling

In order to investigate atomic transport properties and flux coupling phenomena, the self-consistent mean field (SCMF) theory of Nastar has been applied [21]. To discuss transport properties it is useful to rewrite Fick's equations in terms of Onsager transport coefficients (L_{ij}) and gradient of chemical potential ($\nabla\mu_j$), so as to separate the kinetic and thermodynamics contributions. The flux of each considered species can then be written as

$$J_i = -\sum_{j=1}^{N} \frac{L_{ij}}{k_B T} \nabla \mu_j \, . \qquad (1)$$

The SCMF theory relies on using a predefined set of jump frequencies (from ab initio calculations or interatomic potentials) and detailed balance. The jump frequencies are defined as

$$\omega_{ij} = v_{ij} \, exp\left(-\frac{E_{ij}^{m}}{k_B T}\right), \qquad (2)$$

where E_{ij}^{m} is the migration barrier and the *ij* nomenclature is explained in Figures 1 (2) for vacancies (self-interstitials).

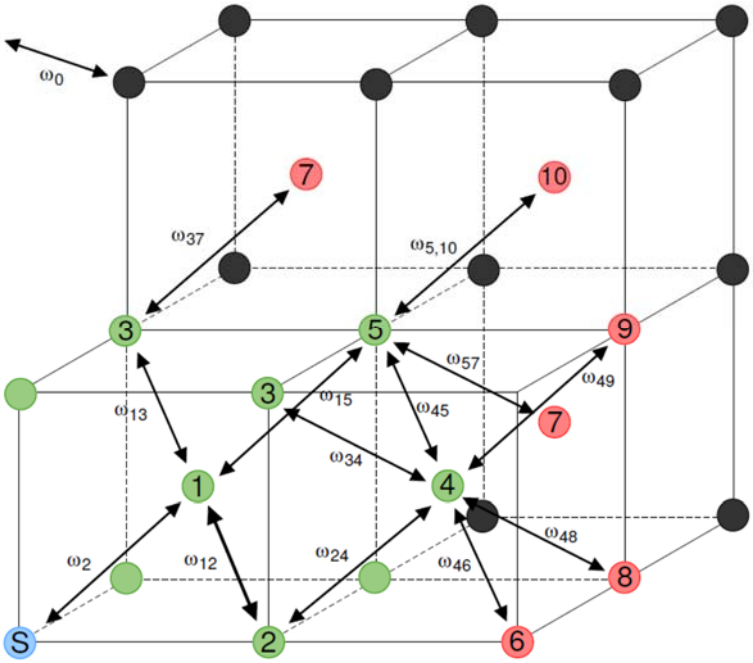

Figure 1. Network of the 12 Fe-V jump frequencies affected by the presence of a solute atom, for solute-vacancy interactions extending to the 5nn distance. The solute-vacancy exchange is labelled ω_2, while ω_0 represents the unaffected Fe-V jump frequency.

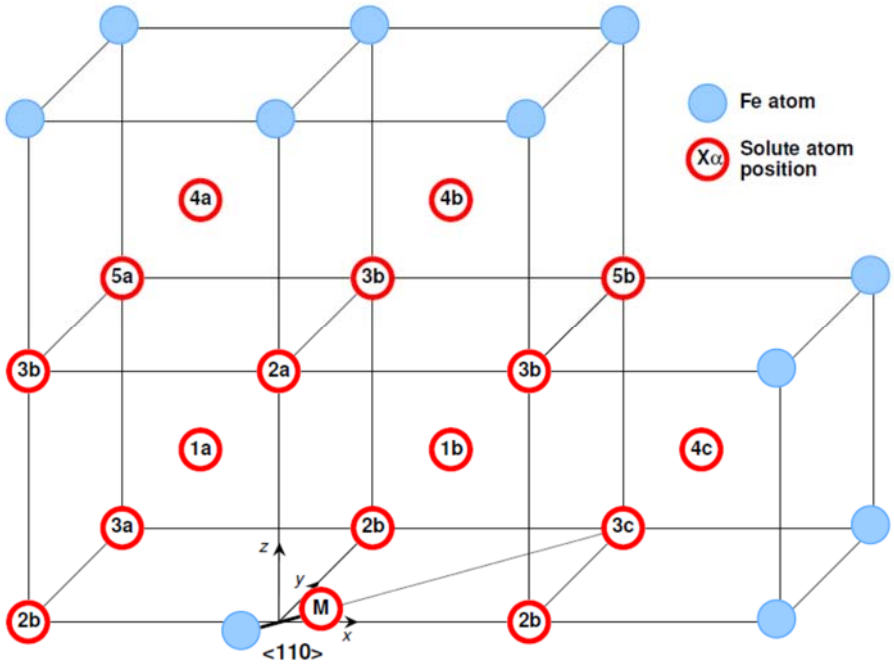

Figure 2. Nomenclature of different dumbbell-solute configurations. In the label $x\alpha$, x is the solute nearest-neighbor position with respect to the dumbbell, whereas α stands for different combinations with respect to the dumbbell orientation. The colored atoms are located outside the interaction shell and the first shell reachable within one jump. The mixed dumbbell configuration is marked with 'M'.

The full details of the SCMF theory can be found in [21] and all details of the application here reported can be found in [4,5].

3. Results

Bulk and defect properties in bcc Fe from DFT have been explored in a number of works [22-25]. In Table 1 we compare the current calculations to previous ones and to experiments for a number of basic bulk- and defect properties. The agreement is very good and eventual discrepancies are discussed in more detail in [4].

Table 1. Bulk properties (computed or adopted in this work), compared with experiments and previous calculations.

Quantity	This work	Previous calculations	Experiments
Lattice parameter a_0	2.831 Å	2.83 Å[a], 2.86 Å[b]	2.86 Å[k]
Vacancy formation enthalpy H_v^f	2.18 eV	2.20 eV[c], 2.02 eV[d], 2.16 eV[e]	1.60 eV[l], 2.0 eV[m]
Vacancy migration energy E_v^{mig}	0.70 eV	0.67 eV[c], 0.65 eV[d]	0.55 eV[n]
Ferromagnetic activation energy Q_v^F	2.88 eV	2.87 eV[c], 2.67 eV[d]	2.95 eV[o], 2.88 eV[l]
Vacancy formation entropy S_v^f	$4.1k_B$[e]	$1.5–2.0k_B$[f], $2.1k_B$[g], $<5\,k_B$[h]	
Attempt frequency ν_0^*	6 THz	91.5 THz[i], 4.9 THz[j]	

References a-o, see Table 1 in [4].

3.1 Solute – vacancy results

The DFT interaction energies of the here considered solutes with vacancies are presented in Figure 3. The results agree well with previous calculations and with available experiments. It is clear that most solutes bind vacancies to some extent, except for Cr where the interaction is very weak.

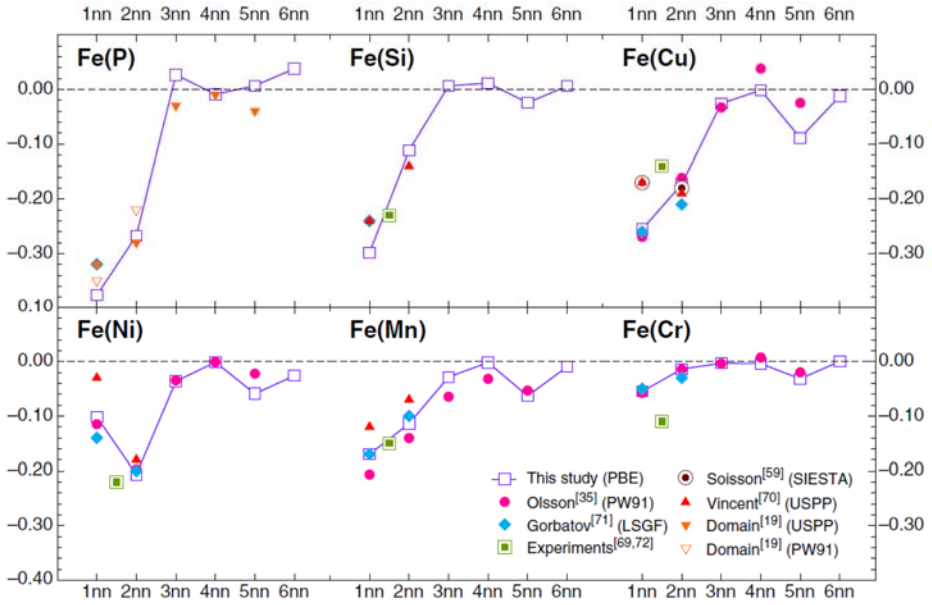

Figure 3. Ab initio solute-vacancy binding energies (in eV) obtained by supercell relaxation, compared with previous calculations and experiments. Negative energies stand for attractive interactions. For references, see Figure 2 in [4].

Moreover, a large database of DFT solute-solute and solute-vacancy interactions has been generated with configurations from first- to fifth nearest neighbour. The interaction tables themselves are present in Appendix A.

The effect of the choice of detail in the transport model is investigated in terms of the solute drag factors for the dilute binary alloys, see Figure 4. Full details in [4]. It is clearly shown here that the simplest choice of first nearest neighbour (1nn) interactions and kinetic pathways is not sufficiently refined to capture the transport properties. Between 2nn and 5nn models the difference is essentially insignificant, however.

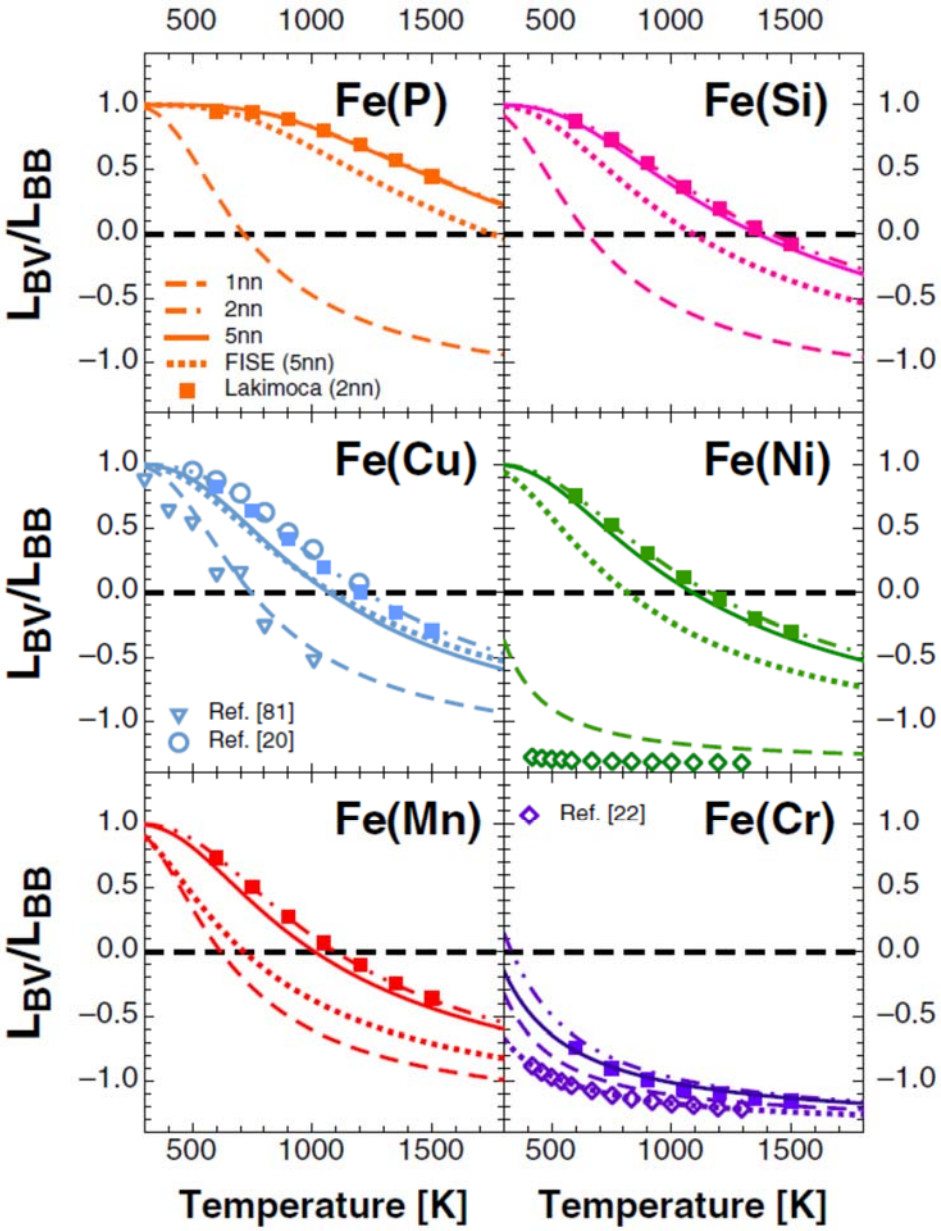

Figure 4. Solute-drag factors $L_{BV}/L_{BB} = -(1+L_{AB}/L_{BB})$ obtained with the SCMF method (lines) and with kinetic Monte Carlo simulations (dots) for each binary alloy, with several jump frequency sets (1nn, 2nn, 5nn, and FISE). Drag occurs for values greater than 0. The 2nn-model curve overlaps with the 5nn-model one for Fe(P). Results of previous works are also shown for Fe(Cr), Fe(Ni), and Fe(Cu). Reference numbering from [4].

The diffusion coefficients for vacancy assisted (thermal) diffusion are presented in Figure 5. The agreement with experiments is very good. Only for Mn is the activation energy visibly different. This is most probably due to the approximated way in which the magnetic phase transition is handled here, assuming that the effect is constrained to that of the Fe lattice.

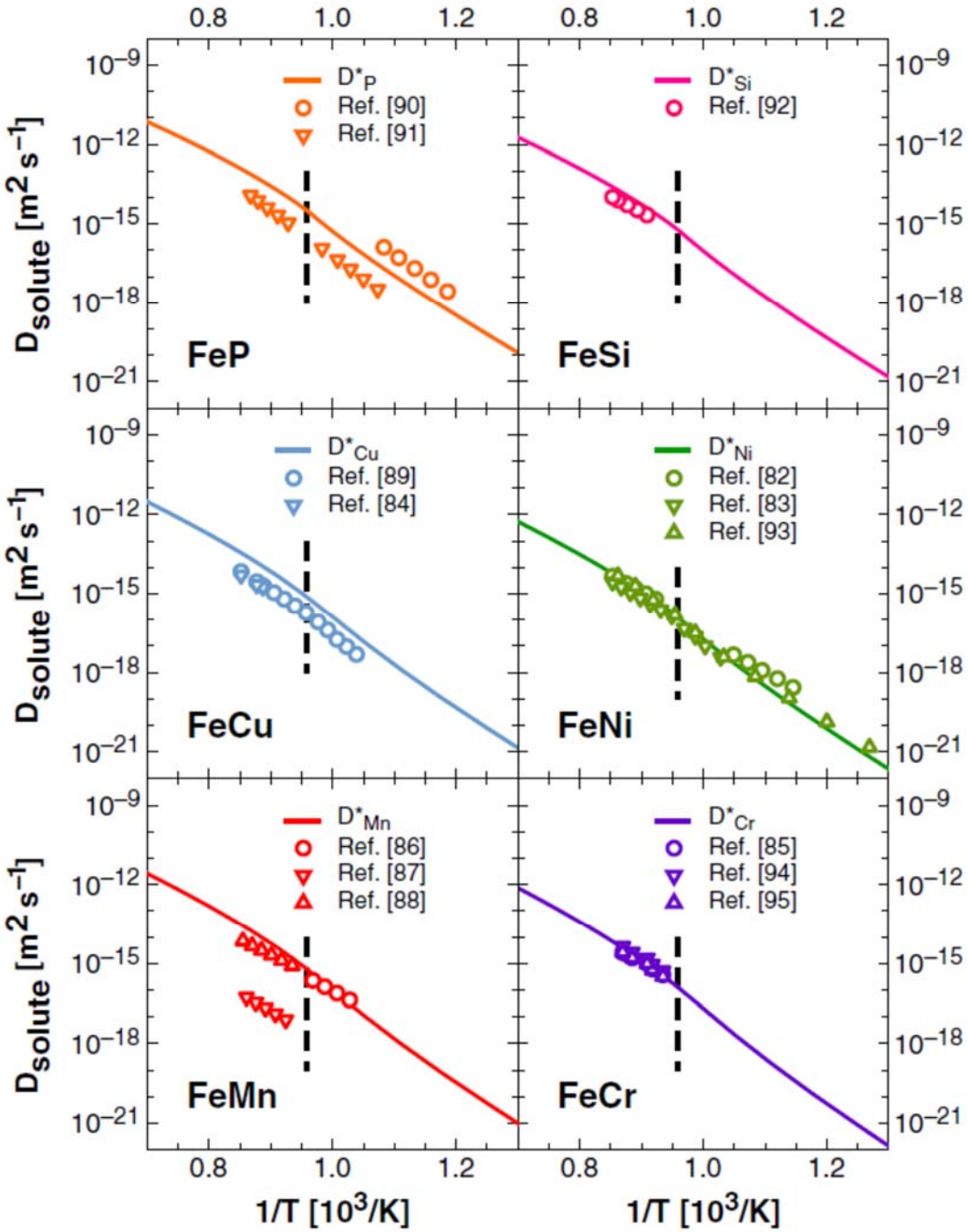

Figure 5. Comparison of solute tracer diffusion coefficients computed with the SCMF method in the 5nn model with experiments. The dashed line marks the magnetic order-disorder transition. Reference numbering from [4].

By calculating the partial diffusion coefficients, radiation induced segregation (RIS) tendencies can be identified, see Figure 6. We see here clearly that in the approximation of negligible effect of SIA diffusion, RIS will drive segregation to e.g. grain boundaries, by vacancies, for all solutes except Cr up to high temperatures.

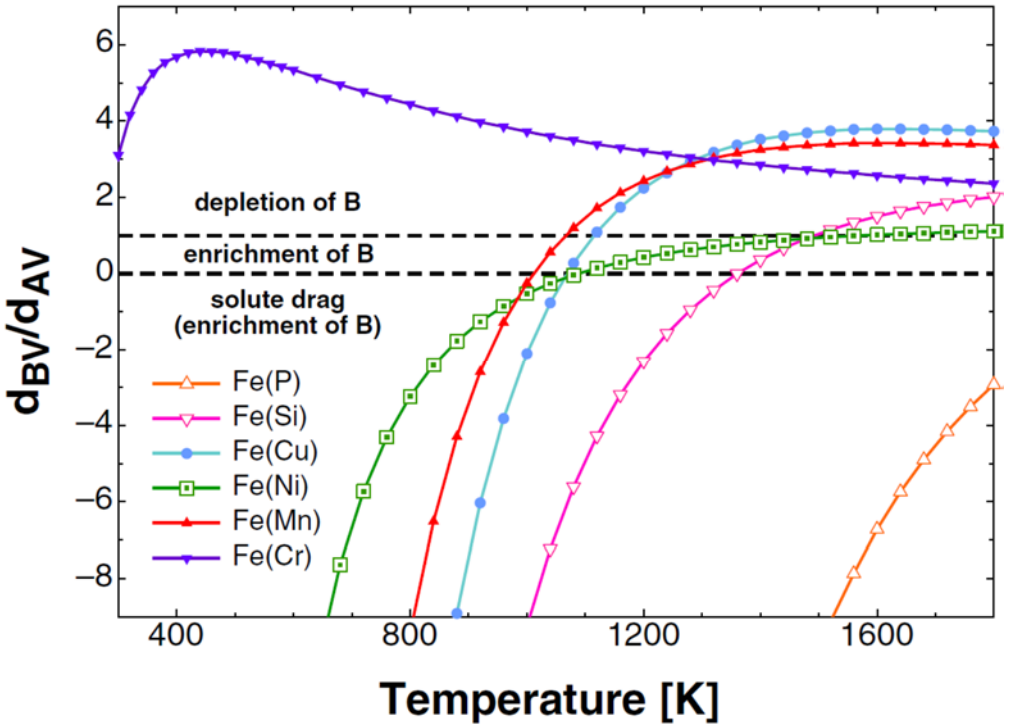

Figure 6. RIS tendencies computed with the SCMF method in the 5nn model, for the Fe-X binary alloys. Solute drag (and subsequent enrichment at sinks) takes place when the ratio is negative; in the opposite case, enrichment holds as long as the ratio is smaller than 1.

3.2 Solute – self-interstitial results

Self-interstitials have been treated in the same way as the vacancies, including a wide range of DFT interaction and migration energy calculations. The full details of the results pertaining to the kinetics and the model development can be found in Paper III of the PhD thesis of L. Messina [5]. The main results will be presented here.

First, however, a wide range of solute-solute – SIA configurations have been considered, in zeroth and first shell configurations, see Appendix B. A model assuming that the total binding energy is dominated by the sum of the two individual solute – SIA interactions for the solute-solute – SIA interactions provide predictions within 0.1 eV of the DFT data for essentially all cases except the zeroth shell configurations (SIA_AB_MM, SIA_AB_Cc, SIA_AB_Cf and SIA_AB_MT), see Appendix B. Even for the latter of these (SIA_AB_MT), the screening introduced by the SIA is so strong that only 6 out of 36 configurations have larger than 0.1 eV errors in prediction. All of these cases have at least one non-transition metal atom (Si or P) in them. Thus, such a simple pair model will capture most of the physics if introduced in, for example, a kinetic Monte Carlo code. The conclusions that can be drawn are that many-body effects are small and simple rules for adding pair interactions work very well for these solutes.

The solutes Si, Cu and Ni do not bind SIAs and therefore their interaction with SIAs is of vanishing importance, as can be seen in the correlation factors presented in Figure 7. For Cr, Mn and P, however, there are significant binding energies and therefore also the SIA diffusion mechanism is activated and plays an important role.

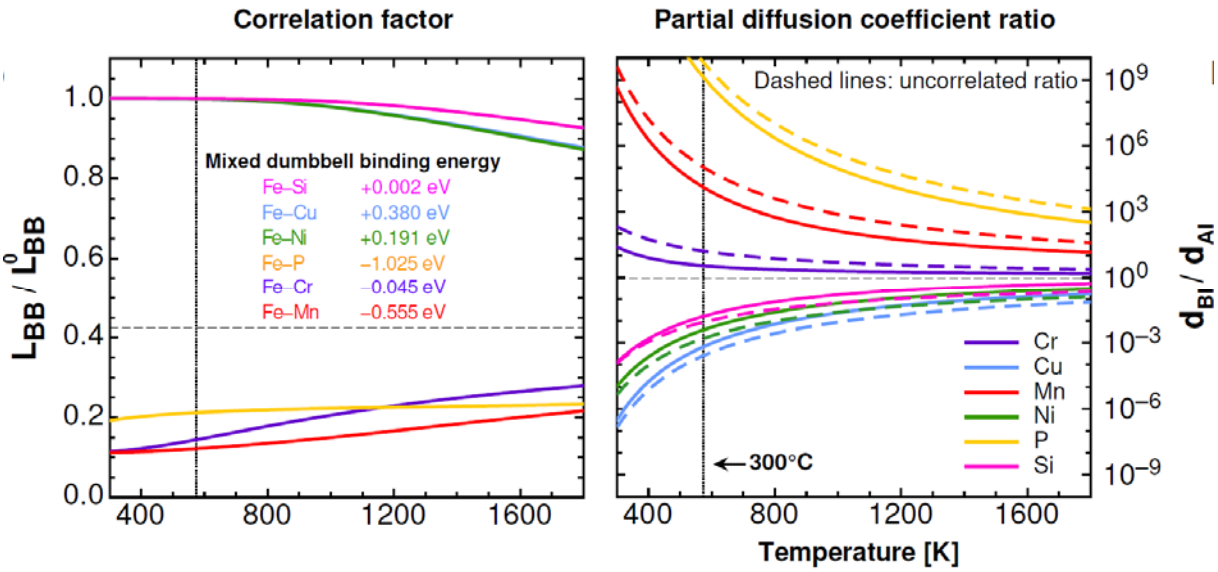

Figure 7. Left) Correlation factor for dumbbell-assisted solute diffusion as a function of temperature, and DFT mixed-dumbbell binding energies (negative values stand for attractive interactions). The dashed line marks the value of the geometric correlation factor $f_0 = 0.42$ for dumbbell diffusion in bcc crystals. Right) Ratio of solute-to-iron partial diffusion coefficients, as a function of temperature. Solute transport by a dumbbell mechanism occurs when the ratio is larger than unity. The dashed lines represent the same quantity when kinetic correlations are not taken into account.

The partial diffusion coefficients for vacancy and SIA driven diffusion are presented in Figure 8 (left), together with the compound RIS tendencies under irradiation conditions where Frenkel pairs are produced (right). For most solutes there is enrichment at sinks due to vacancy (SIA) drag for Cu, Ni, Si, (P, Mn) up to high temperatures. For Cr there is a competition between SIA-driven enrichment and vacancy-driven depletion, leading to a predicted switch-over temperature close to room temperature. This tendency has been seen in experiments on concentrated Fe-Cr alloys: that all solutes enrich except Cr which has a switching behaviour [26].

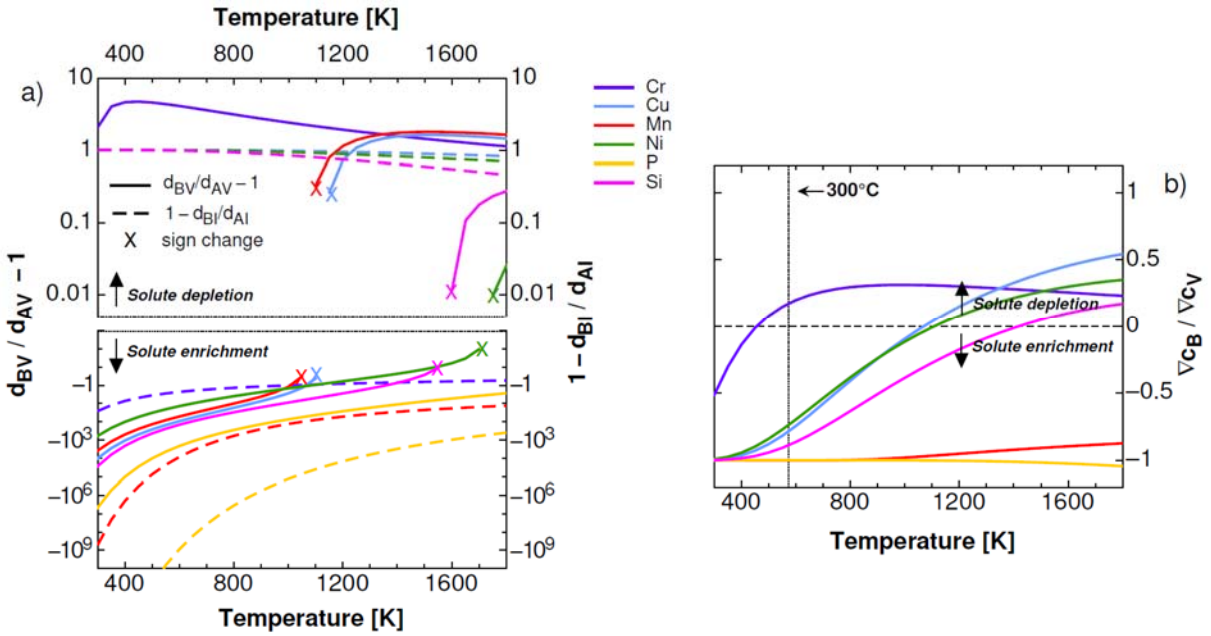

Figure 8. a) Partial diffusion coefficient ratio for vacancy- (solid lines) and interstitial-assisted (dashed lines) diffusion as a function of temperature. The ratios are renormalized in order to have solute depletion in the above panel, and solute enrichment below. The sign change for a few curves is marked with 'X'. b) Global radiation-induced segregation tendencies as functions of temperature.

3.3 Solute – SIA-loop results

For all solutes, the interaction of solutes inside the loop is either negligible or strongly repulsive, see Figure 9. As could be expected, large atoms such as Mo and W, and to a lesser extent V, are also repelled when they are positioned inside the loop. Cr interacts very weakly when situated near the loop edge. Cu, Si and Ni as well as Mn and P are attracted by the loop.

Mn and P can form mixed dumbbells [27,28] and their attraction to the loop is thus quite understandable. The interaction is stronger for P as for the mixed dumbbell.

Ni and Si atoms favour sites in tension and accordingly establish a strong attractive interaction inside the loop. Cu is more stable in sites in compression and it interacts the strongest outside the loop. The small interaction inside the loop at the border is less obvious to understand.

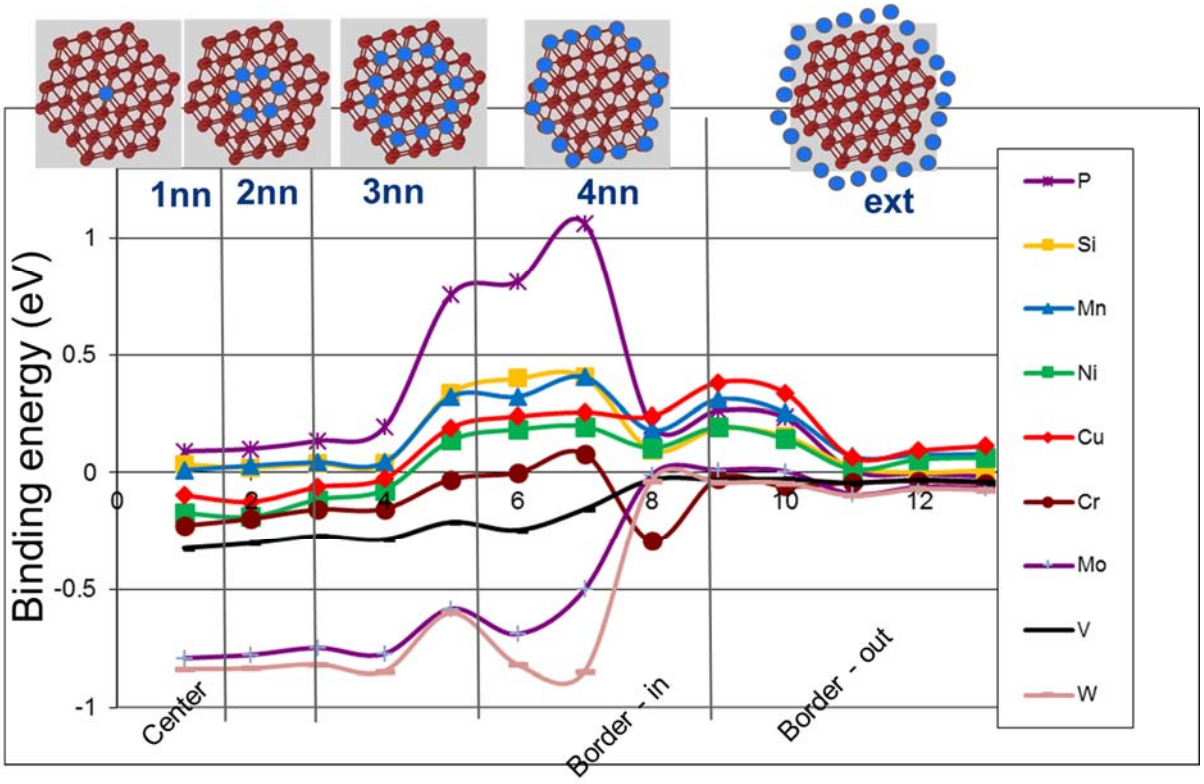

Figure 9. DFT binding energies as function of position for solute atoms to a 37 <111> loop.

The DFT results have been compared for Cu, Ni and Mn with the FeNiMn EAM potential developed by Bonny et al. [29], see Figure 10. The EAM potential underestimates the binding energies and the attraction. Nevertheless using this FeCuNiMn EAM potential, the segregation in interstitial loops has been simulated by Metropolis Monte Carlo [30]. The effect of decorated loops on the dislocation mobility has been evaluated and the unpinning stress was found to be increased mainly for small loops [31].

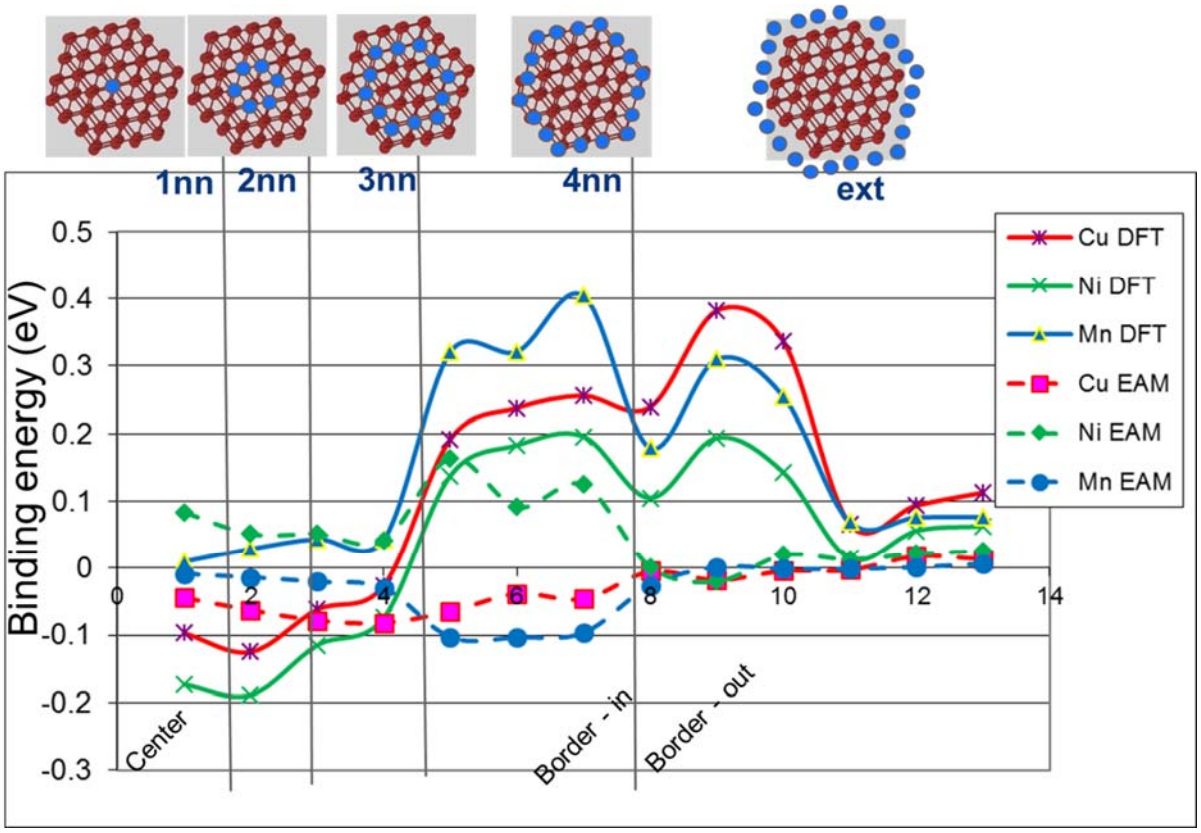

Figure X. Comparison of DFT and EAM binding energies for solute atoms with a 37 <111> loop.

For the <100> loop, the DFT results obtained follow the same trend as for the <111> loop: strong attraction for P mainly inside at the border, large attraction for Mn and Si, see Figure 11. We note strong repulsion for W and Mo inside the loop and weak interaction for Cr with a weak repulsion inside the loop. For Cu and Ni there is a small attraction inside the loop.

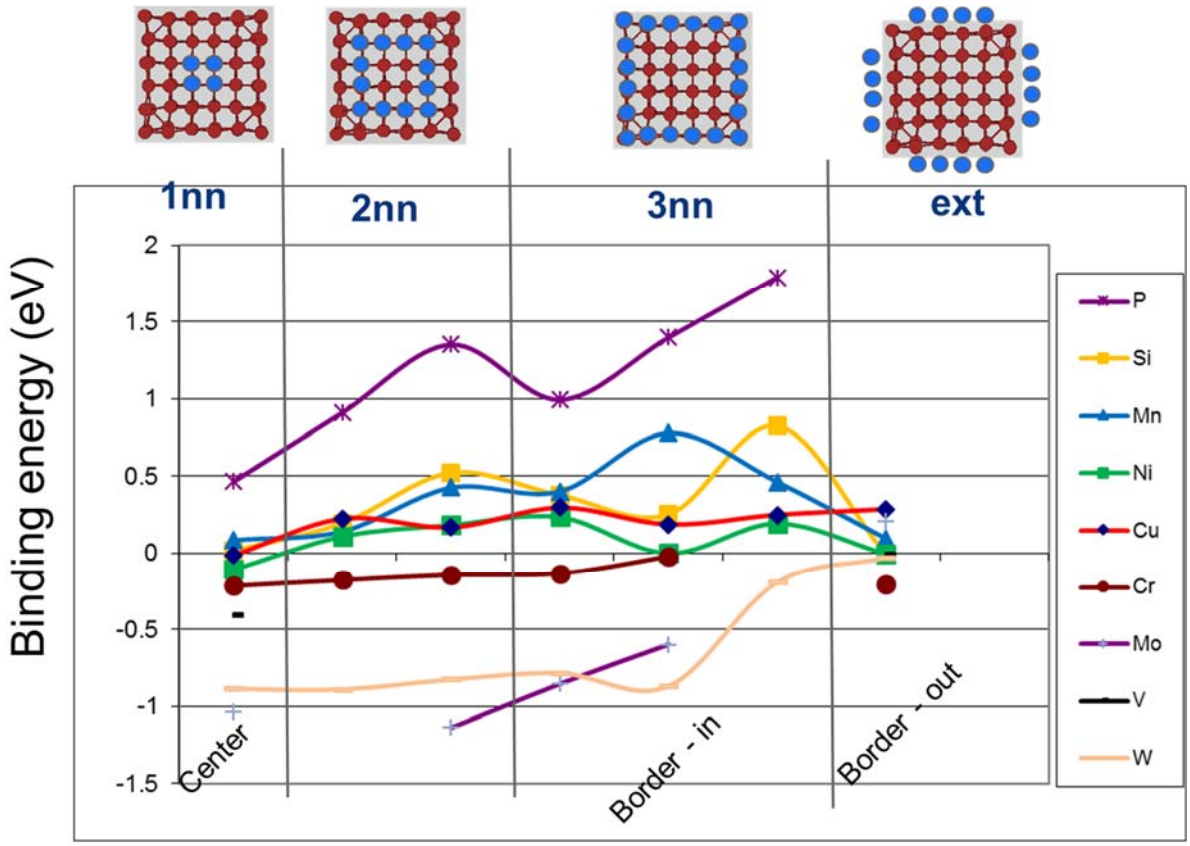

Figure 11. DFT binding energies as function of position for solute atoms to a 36 <100> loop.

4. Conclusions

A wide range of DFT calculations have been performed in this project. The solute-solute interactions are dominated by electronic structure effects rather than elastic ones. The same goes for the solute-defect interactions. For the SIAs, simple pair models work very well to describe the interactions beyond the zeroth shell due to the strong solute-solute screening introduced by the defect.

The vacancies drag all solutes except Cr up to high temperatures (well above the reactor operation range) when correlations become too weak. Solutes are transported by SIAs if the mixed dumbbell is stable. For Cr this introduces a low transition temperature for radiation induced segregation, since there is a competition between SIA enrichment and vacancy depletion.

The solute – SIA-loop interactions are not conforming to expectations from simple arguments. Cr, which is normally bound by SIAs is largely unaffected by loops (slight repulsion), while Cu and Ni have the opposite trends. These results merit further investigation. P, Mn and Si conform more or less to expectations from single SIA-solute predictions.

References

[1] C. Fazio, D. Gomez Briceno, M. Rieth, A. Gessi, J. Henry, L. Malerba, Nucl. Eng. Des. **241** (2011) 3514.
[2] M. Hernandez-Mayoral, L. Malerba, M. Lambrecht, V. Kuksenko, C. Pareige, P. Pareige, F. Bergner, C. Heintze, A. Ulbricht, T. Toyama, M. Ramesh, B. Minov, M. Konstantinović, GETMAT FP7-212175 Deliv. D47 (2013).
[3] M. Hernandez-Mayoral, V. Kuksenko, C. Pareige, P. Pareige, P. Desgardin, B. Décamps, M.-F. Barthe, A. Nordlund, P. Cartemo, A. Idhil, C. Borca, C. Heintze, GETMAT FP7-212175 Deliv. D47 (2013).
[4] L. Messina, M. Nastar, T. Garnier, C. Domain and P. Olsson, Phys. Rev. B **90** (2014) 104203.
[5] L. Messina, Multiscale modeling of atomic transport phenomena in ferritic steels, Doctoral Thesis in Physics, KTH Royal Institute of Technology, Stockholm, Sweden 2015. http://kth.diva-portal.org/smash/get/diva2:873176/FULLTEXT02.pdf
[6] P.E. Blöchl, *Phys. Rev. B* **50**, 17953 (1994); G. Kresse and D. Joubert, *Phys. Rev. B* **59**, 1758 (1999).
[7] J.P. Perdew, K. Burke, and M. Ernzerhof, Phys. Rev. Lett. **77**, 3865 (1996).
[8] J.P. Perdew, J.A. Chevary, S.H. Vosko, K.A. Jackson, M.R. Pederson, D.J. Singh, and C. Fiolhais, Phys. Rev. B **46**, 6671 (1992).
[9] S.H. Vosko, L. Wilk, and M. Nusair, *J. Can. Phys*. **58**, 1200 (1980).
[10] H.J. Monkhorst and J.D. Pack, Phys. Rev. B **13**, 5188 (1976).
[11] G. Mills, H. Jonsson, and G.K. Schenter, Surf. Sci. **324**, 305 (1995).
[12] H. Jonsson, G. Mills, and K.W. Jacobsen, in Classical and Quantum Dynamics in Condensed Phase Simulations, edited by B.J. Berne, G. Ciccotti, and D.F. Coker (World Scientific, Singapore, 1998).
[13] G. Henkelman, B.P. Uberuaga, and H. Jonsson, J. Chem. Phys. **113**, 9901 (2000).
[14] D. Costa, Ph.D. thesis, Université de Sciences et Technologies USTL Lille 1, 2012.
[15] D. Costa, G. Adjanor, C.S. Becquart, P. Olsson and C. Domain, J. Nucl. Mater. **452** (2014) 425.
[16] L. Messina, Z. Chang, and P. Olsson, Nucl. Instrum. Methods Phys. Res. B **303**, 28 (2013).
[17] E. Vincent, C. S. Becquart, and C. Domain, J. Nucl. Mater. **351**, 88 (2006).
[18] P. Pulay, Chem. Phys. Lett. **73**, 393 (1980).
[19] G. P. Kerker, Phys. Rev. B **23**, 3082 (1981).
[20] C. Varvenne, F. Bruneval, M.-C. Marinica and E. Clouet, Phys. Rev. B **88** (2013) 134102
[21] M. Nastar, Philos. Mag. **85**, 3767 (2005).
[22] P. Söderlind, L.H. Yang, J.A. Moriarty, and J.M. Wills, Phys. Rev. B **61**, 2579 (2000).
[23] C. Domain and C. S. Becquart, Phys. Rev. B **65**, 024103 (2001).
[24] C.C. Fu, F. Willaime, and P. Ordejón, Phys. Rev. Lett. **92**, 175503 (2004).
[25] P. Olsson, C. Domain, and J. Wallenius, Phys. Rev. B **75**, 014110 (2007).
[26] J. P. Wharry and G. S. Was, J. Nucl. Mater. **442**, 7 (2013).
[27] E. Vincent, C.S. Becquart, C. Domain, J. Nucl. Mater **382**, 154 (2008).
[28] P. Olsson, T. P.C. Klaver, C. Domain, Phys. Rev. B **81**, 054102 (2010).
[29] G. Bonny, D. Terentyev, A. Bakaev, E.E. Zhurkin, M. Hou, D. Van Neck, L.Malerba, J. Nucl. Mater. **442** (2013) 282.
[30] G. Bonny, D. Terentyev, E.E. Zhurkin, L. Malerba, J. Nucl. Mater. **452**, 486 (2014).
[31] D. Terentyev, X. He, G. Bonny, A. Bakaev, E. Zhurkin, L. Malerba, J. Nucl. Mater. **457**, 173 (2015).

Appendix A

Binding energies (positive = attraction) are reported in units of eV.

DFT data for solute-solute and solute-vacancy pair interactions

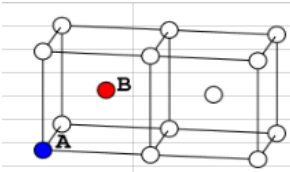

A-B 1nn	Cr	Mn	Ni	Cu	Si	P	vac
Cr	0.2418	-0.0235	0.1062	0.0089	0.0425	-0.0193	-0.0574
Mn		-0.0803	0.0472	0.0360	-0.0191	-0.1949	-0.2064
Ni			-0.0221	-0.1532	-0.1326	-0.1274	-0.1151
Cu				-0.2495	-0.1152	-0.1218	-0.2697
Si					0.3387	0.3235	-0.3061
P						0.2389	-0.3851
vac							-0.1535

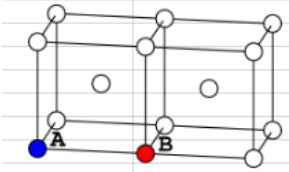

A-B 2nn	Cr	Mn	Ni	Cu	Si	P	vac
Cr	0.1235	0.0053	0.0752	0.0400	0.0842	0.0897	-0.0144
Mn		-0.0381	0.0464	0.0289	-0.0002	-0.0007	-0.1404
Ni			-0.0020	-0.0330	0.0845	0.0340	-0.1967
Cu				-0.0598	0.0021	-0.0723	-0.1615
Si					0.1485	0.1188	-0.1165
P						0.0497	-0.2730
vac							-0.2118

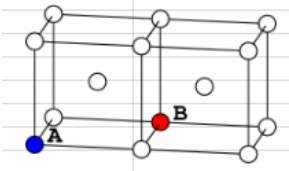

A-B 3nn	Cr	Mn	Ni	Cu	Si	P	vac
Cr	0.0383	0.0087	0.0376	0.0130	0.0099	0.0070	-0.0038
Mn		0.0009	0.0160	-0.0018	-0.0069	-0.0022	-0.0647
Ni			0.0184	0.0038	0.0235	0.0265	-0.0347
Cu				-0.0181	0.0016	-0.0028	-0.0331
Si					-0.0240	-0.0363	0.0051
P						-0.0395	0.0243
vac							0.0114

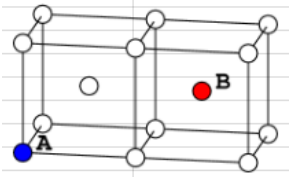

A-B 4nn	Cr	Mn	Ni	Cu	Si	P	vac
Cr	0.0434	0.0161	0.0214	0.0136	0.0273	0.0272	0.0074
Mn		-0.0011	0.0131	0.0062	0.0111	0.0075	-0.0320
Ni			0.0088	0.0022	-0.0012	0.0007	-0.0008
Cu				-0.0121	-0.0199	-0.0171	0.0389
Si					-0.0231	-0.0187	0.0089
P						-0.0222	-0.0105
vac							-0.0420

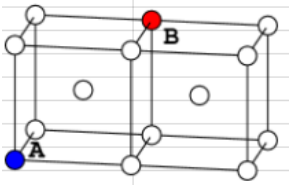

A-B 5nn	Cr	Mn	Ni	Cu	Si	P	vac
Cr	-0.0133	0.0400	0.0102	-0.0118	0.0065	0.0094	-0.0199
Mn		0.0080	0.0060	-0.0090	0.0072	0.0107	-0.0534
Ni			-0.0030	-0.0210	-0.0086	-0.0009	-0.0224
Cu				0.0031	-0.0386	-0.0363	-0.0249
Si					-0.0001	-0.0045	-0.0246
P						-0.0022	0.0070
vac							-0.0556

Appendix B

Binding energies (positive = attraction) are reported in units of eV.

Page 1. DFT data of solute-solute – SIA interactions (1)

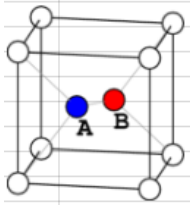

		B						
	SIA_AB_MM	Cr	Mn	Ni	Cu	Si	P	Fe
A	Cr	0.4250						-0.0801
	Mn	-0.3486	-1.0249					-0.6199
	Ni	-0.1643	-0.5334	0.1308				0.2047
	Cu	0.1317	-0.2638	0.2879	0.3015			0.4077
	Si	0.2090	-0.4320	-0.2515	0.0049	0.6167		0.0044
	P	-0.8588	-1.4911	-1.2756	-1.0129	-0.4774	-1.2340	-1.0092
	Fe	-0.0801	-0.6199	0.2047	0.4077	0.0044	-1.0092	

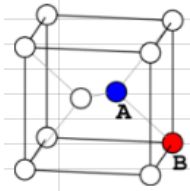

		B						
	SIA_AB_Cc	Cr	Mn	Ni	Cu	Si	P	Fe
A	Cr	0.2087	-0.2333	-0.1734	-0.0728	0.0092	-0.6919	-0.0801
	Mn	-0.4667	-0.8731	-0.6326	-0.5761	-0.6727	-1.3174	-0.6199
	Ni	0.2175	-0.0181	0.0467	-0.0730	-0.2720	-0.7664	0.2047
	Cu	0.4787	0.2100	0.1807	0.0307	0.0622	-0.4172	0.4077
	Si	0.3357	-0.0236	-0.2216	-0.1444	0.5004	0.2203	0.0044
	P	-0.7582	-1.1569	-1.2131	-1.0410	-0.3553	-0.5566	-1.0092
	Fe	-0.0501	-0.3515	-0.0517	-0.0526	-0.2819	-0.8671	

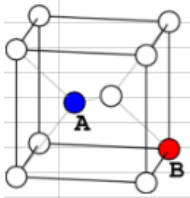

		B						
	SIA_AB_Cf	Cr	Mn	Ni	Cu	Si	P	Fe
A	Cr	-0.1539	-0.4177	-0.1944	-0.1980	-0.3829	-0.9620	-0.0801
	Mn	-0.6617	-0.9170	-0.7086	-0.7089	-0.9072	-1.4647	-0.6199
	Ni	-0.0284	-0.3520	0.1376	0.1840	-0.0964	-0.8138	0.2047
	Cu	0.1277	-0.2234	0.3394	0.3975	0.1339	-0.7846	0.4077
	Si	-0.1996	-0.5391	0.0241	0.0727	-0.3133	-1.1313	0.0044
	P	-1.1760	-1.4831	-1.0238	-1.0077	-1.3784	-2.0828	-1.0092
	Fe	-0.0501	-0.3515	-0.0517	-0.0526	-0.2819	-0.8671	

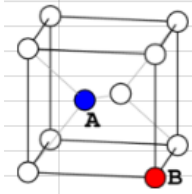

		B						
	SIA_AB_MT	Cr	Mn	Ni	Cu	Si	P	Fe
A	Cr	0.0227	-0.0999	-0.0617	-0.2190	0.0685	0.1777	-0.0801
	Mn	-0.5242	-0.6427	-0.6151	-0.7753	-0.4576	-0.3329	-0.6199
	Ni	0.2794	0.2056	0.1583	0.0015	0.3886	0.5164	0.2047
	Cu	0.4706	0.4099	0.3389	0.2030	0.6171	0.7553	0.4077
	Si	0.0973	-0.0279	0.0307	-0.0714	0.4502	0.5151	0.0044
	P	-0.9557	-1.0551	-0.9718	-1.0792	-0.6450	-0.6100	-1.0092
	Fe	0.0645	-0.0295	-0.0187	-0.1791	0.1607	0.2991	

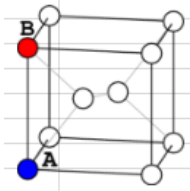

		B						
	SIA_AB_CC2	Cr	Mn	Ni	Cu	Si	P	Fe
A	Cr	-0.1181	-0.4105	-0.0763	-0.0839	-0.3164	-0.8869	-0.0501
	Mn		-0.6872	-0.3949	-0.4202	-0.6355	-1.1911	-0.3515
	Ni			-0.1113	-0.1369	-0.3403	-0.9288	-0.0517
	Cu				-0.1383	-0.3186	-0.9228	-0.0526
	Si					-0.5157	-1.0886	-0.2819
	P						-1.6149	-0.8671
	Fe							

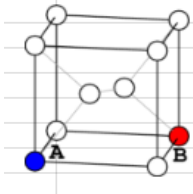

		B						
	SIA_AB_CC3	Cr	Mn	Ni	Cu	Si	P	Fe
A	Cr	-0.1543	-0.4458	-0.0844	-0.1001	-0.3707	-0.9618	-0.0501
	Mn		-0.7157	-0.4049	-0.4364	-0.6775	-1.2396	-0.3515
	Ni			-0.1028	-0.1027	-0.3140	-0.8970	-0.0517
	Cu				-0.0804	-0.3049	-0.9164	-0.0526
	Si					-0.5770	-1.1774	-0.2819
	P						-1.7394	-0.8671
	Fe							

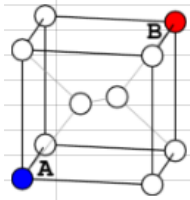

		B						
	SIA_AB_CC5	Cr	Mn	Ni	Cu	Si	P	Fe
A	Cr	-0.1186	-0.4110	-0.0761	-0.0852	-0.3181	-0.8870	-0.0501
	Mn		-0.6876	-0.3952	-0.4203	-0.6361	-1.1903	-0.3515
	Ni			-0.1111	-0.1351	-0.3407	-0.9278	-0.0517
	Cu				-0.1379	-0.3197	-0.9218	-0.0526
	Si				3.3798	-0.5157	-1.0875	-0.2819
	P						-1.6143	-0.8671
	Fe							

Page 2. DFT data of solute-solute – SIA interactions (2)

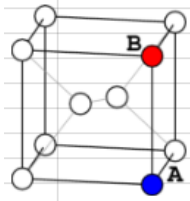

		B						
	SIA_AB_TT2	Cr	Mn	Ni	Cu	Si	P	Fe
A	Cr	0.1951	-0.0091	0.0734	-0.0697	0.2946	0.4444	0.0645
	Mn		-0.0779	-0.0426	-0.2078	0.0894	0.2345	-0.0295
	Ni			-0.0218	-0.1815	0.2293	0.3268	-0.0187
	Cu				-0.3584	0.0424	0.1120	-0.1791
	Si					0.4689	0.5533	0.1607
	P						0.5754	0.2991
	Fe							

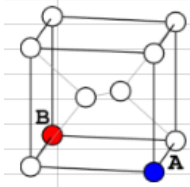

		B						
	SIA_AB_TT3	Cr	Mn	Ni	Cu	Si	P	Fe
A	Cr	0.1208	0.0800	0.0307	-0.1281	0.2249	0.3638	0.0645
	Mn		-0.0089	-0.0431	-0.2061	0.1312	0.2735	-0.0295
	Ni			-0.0675	-0.2088	0.1624	0.2987	-0.0187
	Cu				-0.3460	0.0061	0.1400	-0.1791
	Si					0.3084	0.4319	0.1607
	P						0.5683	0.2991
	Fe							

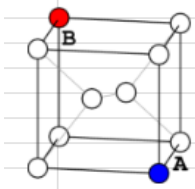

		B						
	SIA_AB_TT5	Cr	Mn	Ni	Cu	Si	P	Fe
A	Cr	0.1235	0.0327	0.0522	-0.0991	0.2244	0.3623	0.0645
	Mn		-0.0026	-0.0531	-0.2139	0.1334	0.2666	-0.0295
	Ni			-0.0001	-0.1688	0.1471	0.2913	-0.0187
	Cu				-0.3458	-0.0243	0.1185	-0.1791
	Si					0.3024	0.4322	0.1607
	P						0.5548	0.2991
	Fe							

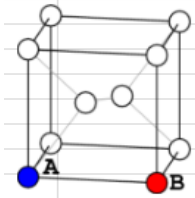

		B						
	SIA_AB_CT2	Cr	Mn	Ni	Cu	Si	P	Fe
A	Cr	0.0433	-0.0902	-0.0495	-0.2101	0.1334	0.2849	-0.0501
	Mn	-0.2725	-0.3230	-0.3590	-0.5285	-0.1715	-0.0429	-0.3515
	Ni	0.0343	-0.0563	-0.0871	-0.2640	0.0926	0.1556	-0.0517
	Cu	0.0184	-0.0629	-0.1091	-0.2696	0.0458	0.1018	-0.0526
	Si	-0.1923	-0.2468	-0.3115	-0.4730	-0.1429	-0.0488	-0.2819
	P	-0.7746	-0.8905	-0.9381	-1.1024	-0.8408	-4.0998	-0.8671
	Fe	0.0645	-0.0295	-0.0187	-0.1791	0.1607	0.2991	

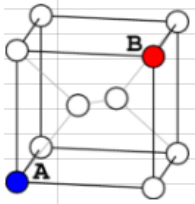

		B						
	SIA_AB_CT3	Cr	Mn	Ni	Cu	Si	P	Fe
A	Cr	0.0390	-0.0594	-0.0522	-0.2132	0.1297	0.2502	-0.0501
	Mn	-0.2674	-0.2892	-0.3473	-0.5105	-0.1775	-0.0683	-0.3515
	Ni	0.0290	-0.0041	-0.0537	-0.2225	0.1068	0.2444	-0.0517
	Cu	0.0286	-0.0771	-0.0556	-0.2146	0.0938	0.2246	-0.0526
	Si	-0.2082	-0.3073	-0.2871	-0.4596	-0.1468	-0.0133	-0.2819
	P	-0.8179	-0.8939	-0.8704	-1.0377	-0.7189	-0.6000	-0.8671
	Fe	0.0645	-0.0295	-0.0187	-0.1791	0.1607	0.2991	